High-magnetic-field EPR of Cr-based diluted magnetic semiconductors

M. E. J. Boonman*
Research Institute for Materials, High Field Magnet Laboratory, University of Nijmegen, Toernooiveld, NL-6525 ED, Nijmegen, The Netherlands

W. Mac and A. Twardowski
Institute of Experimental Physics, Warsaw University, Hoża 69, PL-00-681 Warsaw, Poland

A. Wittlin
Research Institute for Materials, High Field Magnet Laboratory, University of Nijmegen, Toernooiveld, NL-6525 ED, Nijmegen, The Netherlands
and Institute of Physics, Polish Academy of Sciences, Warsaw, Poland

P. J. M. van Bentum and J. C. Maan
Research Institute for Materials, High Field Magnet Laboratory, University of Nijmegen, Toernooiveld, NL-6525 ED, Nijmegen, The Netherlands

M. Demianiuk
Institute of Technical Physics, WAT, 00908, Warsaw, Poland
(Received 28 September 1999)

We have studied magnetic interactions in chromium-based diluted magnetic semiconductors by measuring in detail the electron paramagnetic resonance spectrum of Cr^{2+} over the frequency range between 30 and 210 GHz at high magnetic fields up to 20 T oriented along different crystal axes. At low temperatures, crystals of chromium-alloyed zinc chalcogenides $Zn_{1-x}Cr_x$ (S, Se, Te) demonstrate complex properties that are neither of Brillouin nor of Van Vleck type. The behavior of these Cr^{2+} impurities in semimagnetic materials results from the interaction of the ground state with the low-lying electronic states of the $3d$ Cr^{2+} ion and from the Jahn-Teller-induced distortion of the Cr^{2+} position in the host lattice. We measured optical transitions between these states and we could determine the magnetic-field dependence and the anisotropy of the electronic levels. We explain our results with the crystal-field model proposed by Vallin *et al.*,[1] including a cubic crystal field and Jahn-Teller distortion, and we evaluate the dependence of the model parameters on the semiconductor host lattice.

I. INTRODUCTION

Diluted magnetic semiconductors (DMS) or semimagnetic semiconductors are classical semiconductors (such as CdTe, ZnSe, or InAs), where a controlled fraction of the nonmagnetic cations is randomly substituted by magnetic ions of transition metals or rare earth metals.[2–4] The combination of the physics of semiconductors and magnetism in these materials has attracted a lot of research, because of the interaction between the delocalized band electrons and localized electrons of the magnetic ions.[5,6] The magnetic properties of these materials are directly related to the localized magnetic moments on the substituted ions, and thus depend on the energy level scheme of the magnetic ion in the nonmagnetic host lattice. These properties of DMS were extensively studied for Mn^2 or Fe (Ref. 7) substitutes, mostly in II-VI host materials.

Substitutional Mn for example shows typical Brillouin paramagnetism, since the magnetic moment of the Mn^{2+} ion in the ground state, a degenerate multiplet, results solely from the spin (d^5; $L=0$, $S=5/2$).[8,9]

The Fe^{2+} ion has a nonvanishing orbital momentum (d^6; $L=2$, $S=2$),[9,10] and therefore a magnetic moment in the singlet ground state can only be induced by a magnetic field, which leads to the so called Van Vleck-type paramagnetism. In this paper, we concentrate on the synthesized class of Cr-based DMS. The Cr^{2+} ion also has a nonvanishing orbital momentum (d^4; $L=2$, $S=2$).[1,9] However, the multiplet ground state consists of nearby states within an energy range of 10 cm^{-1}, which is different from all other known DMS. These Cr-based DMS represent an intermediate case between the Brillouin and Van Vleck type of paramagnetism, since the excited states of the Cr^{2+} ion are energetically close enough to contribute to the magnetic properties. Moreover, the Cr^{2+} ion is strongly influenced by the static Jahn-Teller effect, which is negligible for the other mentioned substituents and which leads to a pronounced anisotropy of the Cr^{2+} ion energy level structure. Also the magnetic properties are strongly anisotropic, as demonstrated by magnetization and specific heat measurements.[11,12]

Electron paramagnetic resonance studies to map the energy-level scheme in detail in high-magnetic fields (0-20 T) were very difficult due to the lack of appropriate measuring techniques with tunable high frequencies sources (30-210

GHz). With a millimeter wave-vector network analyzer[13] (MVNA) in combination with a resonant cavity technique,[14,15] it has become possible to conveniently perform spectroscopy in the energy range between 1 and 7 cm^{-1}, bridging the gap between the conventional electron paramagnetic resonance (EPR) and far infrared spectroscopy. The heterodyne detection of the MVNA also facilitates the simultaneous measurement of the amplitude and phase of the complex signal, which are directly related to the absorption and dispersion of the electron paramagnetic resonances, see also Refs. 16 and 17. In this paper, we will start by discussing the experimental circumstances of the measurements in Sec. II. Section III will show the obtained experimental results for $Zn_{1-x}Cr_xTe$, $Zn_{1-x}Cr_xSe$, and $Zn_{1-x}Cr_xS$. The theoretical description of the data, a crystal-field model, will be presented in Sec. IV. In Sec. V, we will discuss the experimental results for $Zn_{1-x}Cr_xTe$, $Zn_{1-x}Cr_xSe$, and $Zn_{1-x}Cr_xS$ in magnetic fields up to 20 T in the context of the model, and the last section will contain a summary with the main conclusions.

II. EXPERIMENTAL SETUP

A. Samples

The experiments were performed on samples obtained from bulk crystals of $Zn_{1-x}Cr_xTe$, $Zn_{1-x}Cr_xSe$, and $Zn_{1-x}Cr_xS$ grown by the modified high pressure Bridgman technique,[18] using high-purity ZnTe, ZnSe, or ZnS and pure metallic chromium. Instead of metallic chromium a high purity CrSe was used for some of the $Zn_{1-x}Cr_xSe$ samples. The chromium concentration of the obtained single phase monocrystals was rather low, for $Zn_{1-x}Cr_xSe$ and $Zn_{1-x}Cr_xS$ $x<0.007$ and $x<0.001$ for $Zn_{1-x}Cr_xTe$. The chromium concentration was determined using atomic absorption, electron microprobe, and wet chemical analysis. Also, low-temperature magnetization measurements provided an accurate relative concentration value.[11] Standard x-ray backscattering analysis provided the information about the crystalline structure of the samples and was used to orient the samples. The largest monocrystalline pieces, cut from the $Zn_{1-x}Cr_xS$ ingots and used in our experiments, were a few millimeter in size. The samples originated from two different ingots with chromium compositions of $x=0.006$ and $x=0.004$. The x-ray investigations showed that this material was neither pure cubic (zinc-blende structure) nor pure hexagonal (wurzite structure) but polytypical (mixed). The crystalline structure of the $Zn_{1-x}Cr_xSe$ crystals appeared to be zinc blende, but with very small grains misoriented relative to each other by about 2-3 degrees. The $Zn_{1-x}Cr_xSe$ samples we measured come from different ingots with chromium concentrations in the range $0.001<x<0.004$. The two different $Zn_{1-x}Cr_xTe$ samples that we studied have a pure cubic crystalline structure and contain chromium in a concentration less than 0.001.

B. Measuring technique

Electron paramagnetic resonances of the Cr^{2+} ions in our samples were measured using a millimeter wave vector network analyzer[13] (MVNA) which is attached to an oversized resonant cavity. The MVNA is an instrument generating and measuring the amplitude and the phase of a millimeter wave signal between 30 and 210 GHz using a solid-state-based vector analyzer with heterodyne detection. The continuously variable YIG frequency between 8 and 18 GHz is guided to frequency multiplying Schottky diodes via coaxial cables allowing a large flexibility of the system, see Fig. 1.

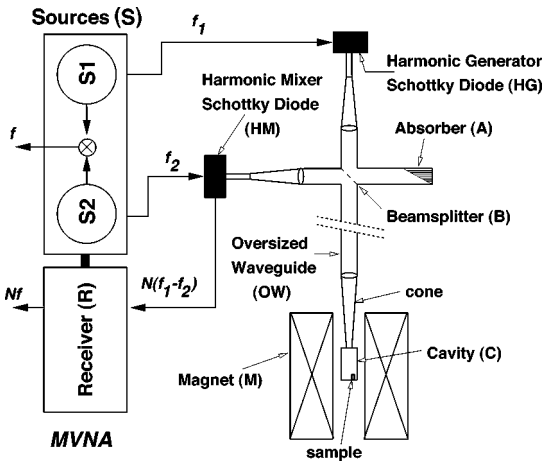

FIG. 1. Schematic overview of the setup used for millimeter wave spectroscopy. On the left-hand side the sources (S), $S1$ and $S2$, together with the receiver (R) form the MVNA. The microwaves are coaxially transmitted to the Schottky diodes harmonic generator [(HG) and harmonic mixer (HM)] connected to the oversized wave-guide system (OW). The cavity (C) containing the sample is placed at the end of the wave guides in the center of the magnet (M).

The millimeter wave radiation coming from the harmonic generator (HG) is quasi-optically guided with oversized cylindrical wave guide (OW) (light pipe) to the magnetic field center, where the wave guide is coupled to an oversized resonant cavity (C). With a mylar beamsplitter (B) part of the reflected radiation is coupled to the harmonic mixer (HM) in the horizontal part of the waveguide. With an oversized cylindrical copper cavity ($l=20$ mm, $d=12.5$ mm) and with the advantage of a continuously tunable radiation source, we can study the resonances at one of the many resonant cavity modes over a wide range of frequencies and stabilize this frequency with an external frequency counter.

This tunability is important for studying EPR with zero field split levels or with a strong nonlinear magnetic-field dependence of line positions. In these cases, like for the Cr^{2+} ion in our samples, a measurement at a single frequency is not conclusive. The vector detection of the MVNA is particularly useful in more accurately determining the resonance line shape and more successful in discriminating between two closely lying resonances than scalar detection. We used direct detection of the millimeter wave signal, in contrast to most EPR spectrometers, which use magnetic field modulation to enhance the sensitivity.

The observed ''vector'' signal consists of a resonant part, and a nonresonant background (complex ''leak signal'') which is not influenced by the sample. Fitting an observed resonance with a circle in polar coordinates (with r the amplitude and ϕ the phase of the signal), assuming a Lorentzian line shape, we find the value of this complex ''leak signal,'' which can be subsequently subtracted from the measured signal.[17] If the cavity is tuned to resonance and the wave-

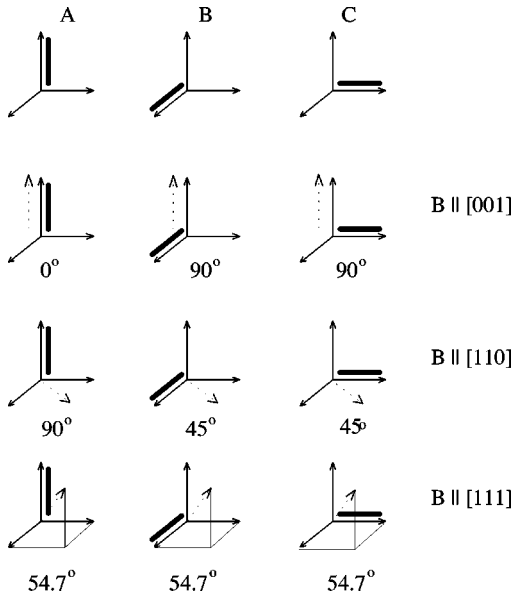

FIG. 2. The three different types of Cr centers depending on the direction of the magnetic field with respect to the Jahn-Teller distortion axis. Thick lines represent the Jahn-Teller distortion axis and dashed lines indicate the magnetic field direction.

guide system is not in resonance at the same frequency, the measured response will be the signal from the sample times a complex multiplication factor. After correcting the amplitude and phase signal, assuming the leak signal and complex scaling factor are constant over the whole measurement, we obtain two signals corresponding to the absorption respectively dispersion of the sample.

The complex signal also provides information about the sign of the energy versus magnetic field slope, it allows to distinguish between transitions whose energy increases or decreases with magnetic field. This is a consequence of the opposite sign of phase change rate in both cases. Therefore, the vector signal follows the resonance in the polar plane clockwise or counterclockwise with increasing magnetic field depending on the sign of the energy slope.

C. Experimental conditions

In all our measurements, the sample was mounted on the bottom of the resonant cavity placed in the center of the static magnetic field. Resonances in the reflected millimeter wave signal were measured at constant frequency (energy) as function of magnetic field. The magnetic field was supplied by either a superconducting coil ($\mathbf{B} \leqslant 18.5$ T) or a Bitter magnet ($\mathbf{B} \leqslant 20$ T). The samples were oriented such that the magnetic field was applied along either the ⟨100⟩, ⟨110⟩, or ⟨111⟩ crystallographic axis of the sample,[19] see Fig. 2.

All presented measurements were done at $T \approx 1.2$ K, in which case only the lowest energy level of Cr^{2+} is populated ($k_B T \approx 1$ cm^{-1}). The behavior of the Cr^{2+} ion energy level pattern in a magnetic field strongly depends on the angle between the field direction and the Jahn-Teller distortion axis. In a cubic crystal there are generally three equivalent ⟨100⟩ directions, [100], [010] and [001], leading to three types of tetragonally distorted Cr centers, named *A*, *B*, and *C* in Fig. 2. In the absence of a magnetic field the three types of centers are indistinguishable, which is also the case for the magnetic field along the ⟨111⟩ crystal axis, since the angle between the Jahn-Teller distortion axes and field direction is 54.7° for all three centers. For all the other magnetic field directions the three types of centers are inequivalent. In particular for $\mathbf{B} \| \langle 100 \rangle$ the *A* center is distorted parallel to the field direction, the ''0°'' configuration, and centers *B* and *C* are distorted perpendicular to the field, representing the ''90°'' configuration. For the magnetic field $\mathbf{B} \| \langle 110 \rangle$, two centers are in the ''45°'' configuration (*A* and *B*), and one center is distorted perpendicular to the field (*C*).

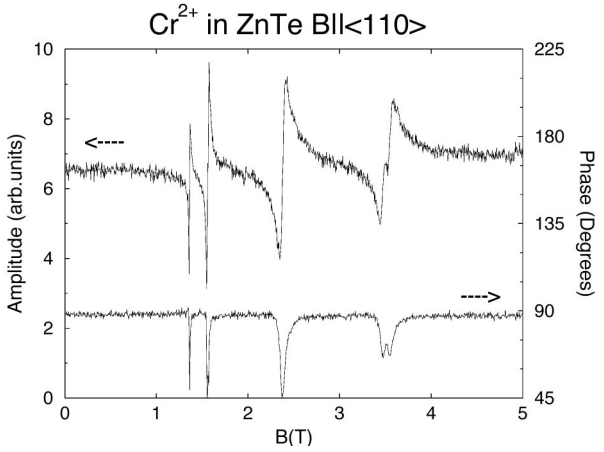

FIG. 3. Measured complex EPR signal (amplitude and phase) at $f = 137.875$ GHz, $T = 1.2$ K and for $B \| \langle 110 \rangle$ (Ref. 20).

III. RESULTS

A. $Zn_{1-x}Cr_xTe$

An example of an electron paramagnetic resonance measurement of $Zn_{1-x}Cr_xTe$, where the magnetic field was oriented along the ⟨110⟩ direction, is depicted in Fig. 3, which shows the amplitude and phase of the complex reflected signal as a function of the applied field.

Several resonances can clearly be observed in both amplitude *r* and phase ϕ although their shape is not typical absorption respectively dispersion like. After the vectorial analysis of the signals, as described before,[17] we can plot the amplitude and phase again as a function of the magnetic field. We get two signals representing the absorption and dispersion of the electron paramagnetic resonances, see Fig. 4.

Figure 5 shows several absorption spectra taken at different increasing (bottom to top) frequencies for the field along the ⟨110⟩ direction. The experimental traces show the presence of three different types of inequivalent Cr^{2+} centers. The first as well as the third resonance in every measurement is a single resonance originating from a ''90°'' configuration center, whereas the second and fourth resonance are always split in two resonances. Two types of Cr^{2+} centers distorted at an angle of 45° and a small misorientation of the sample (below 5°) with respect to the magnetic field, leads to this splitting. EPR measurements at several different frequencies for the field along the ⟨100⟩ direction are displayed in Fig. 6.

In this case, resonances can be observed from two ''90°'' configurations and one ''0°'' configuration Cr^{2+} center. One can see that the background signal is not constant. The sub-

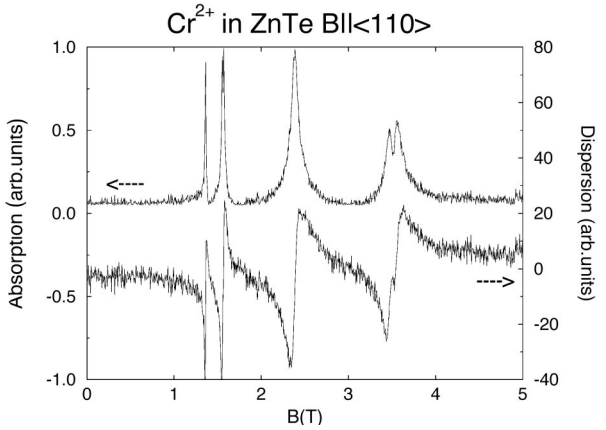

FIG. 4. Transformed EPR signals of Fig. 3 after subtraction of a ''leak signal'' and a complex normalization.

tracted ''leak'' signal was determined at low-magnetic field, whereas with increasing magnetic field the zero-field-tuned cavity is drifting out of resonance. Since we measure at fixed frequency this causes the absorption signal to increase and also changes the dispersion signal. This cavity drift may be caused by the use of a somewhat large sample, together with the changing magnetic susceptibility of the sample with increasing magnetic field.

B. $Zn_{1-x}Cr_xSe$

Figure 7 shows EPR spectra of a Cr^{2+} ion in ZnSe for several different frequencies, with the magnetic field along the $\langle 100 \rangle$ direction. The resonances can clearly be followed as function of frequency (energy) in both absorption and dispersion. At high frequencies, some new resonances appear at low-magnetic fields. These low-field transitions have opposite energy versus magnetic field slopes, which can be deduced from the dispersion curves, where they are each others mirror images (Fig. 8). Moreover, we can derive from this that the two resonances in the 167 GHz measurement correspond to transitions between the same levels. Absorption

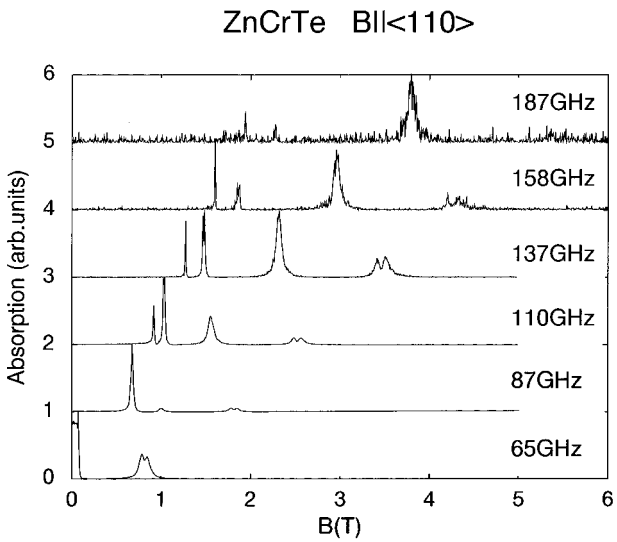

FIG. 5. EPR absorption measurements of $Zn_{1-x}Cr_xTe$ measured with $B \| \langle 110 \rangle$, $T = 1.2$ K and at indicated frequencies. All spectra are normalized and have offsets for clarity.

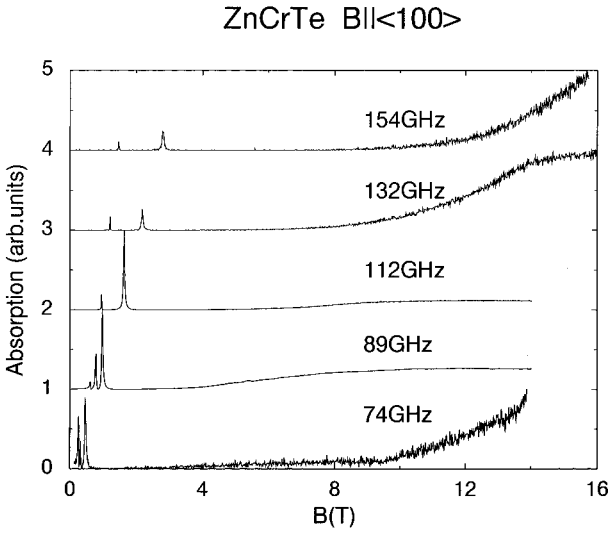

FIG. 6. EPR absorption spectra for different frequencies, measured on $Zn_{1-x}Cr_xTe$ at $T = 1.2$ K and with $B \| \langle 100 \rangle$. All spectra are scaled and have offsets for clarity.

traces alone cannot give indications for this. The very small resonances that are observed at low magnetic fields and frequencies below 160 GHz, originate from transitions between excited levels, which can give an explanation for their small relative intensities.

C. $Zn_{1-x}Cr_xS$

The measurements on $Zn_{1-x}Cr_xS$ were performed with the magnetic field parallel to the $\langle 110 \rangle$ direction. Figure 9 displays the transformed measurements. The data on $Zn_{1-x}Cr_xS$ are taken with free running (not stabilized) YIG oscillators, in contrast to the other externally frequency locked measurements. This results in some noise added to the shown $Zn_{1-x}Cr_xS$ measurements compared to the previous ones on $Zn_{1-x}Cr_xSe$ and $Zn_{1-x}Cr_xTe$. At every frequency we observe next to a strong resonance a small satel-

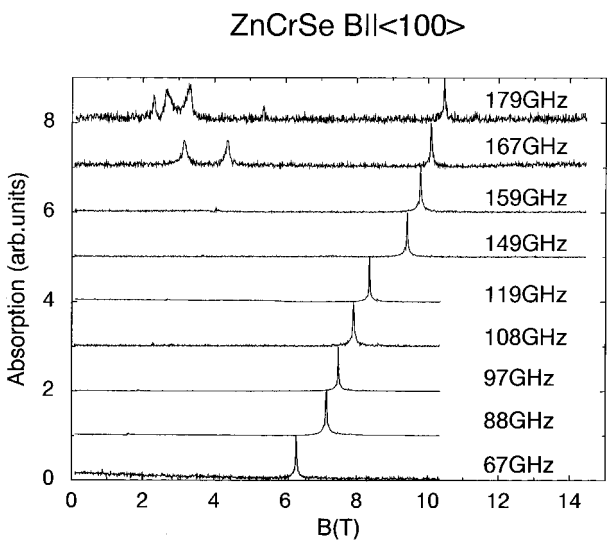

FIG. 7. EPR absorption spectra taken at different frequencies on $Zn_{1-x}Cr_xSe$ at $T = 1.2$ K and with $B \| \langle 100 \rangle$. All spectra are scaled and have offsets for clarity.

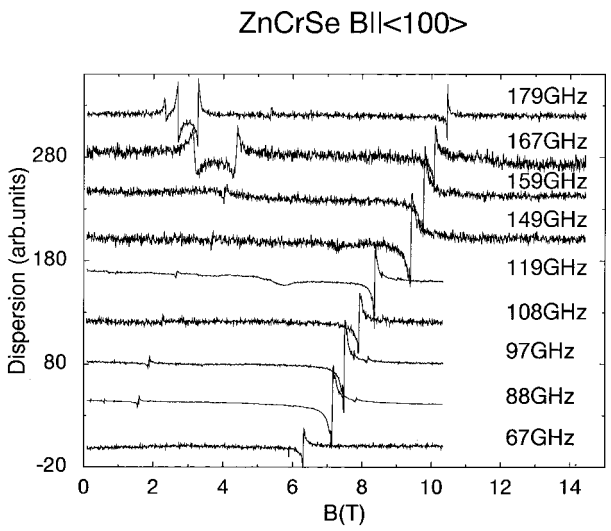

FIG. 8. EPR dispersion spectra corresponding to Fig. 7.

lite resonance at slightly lower magnetic fields. Other experiments and orientations of the crystal, see Ref. 21, show that all observed lines appear in such pairs, except those whose intensity is too weak. A slight misorientation can split a resonance into two resonances if it is originating from two distinct Cr^{2+} centers. This is not the case in our $Zn_{1-x}Cr_xS$ measurements, because the resonance at high-magnetic fields originates from a single center in the ''90°'' configuration. Comparing different orientations of the magnetic field with respect to the Jahn-Teller distortion axis also excludes the possibility of misoriented grains in the samples. The most probable reason for the satellite resonances is the polytypism of the $Zn_{1-x}Cr_xS$ crystals, which gives different types of centers due to different hexagonal stresses. This is confirmed by infrared measurements on polytypical $Zn_{1-x}Cr_xS$.[1]

IV. THEORETICAL DESCRIPTION

A. The energy levels of a Cr^{2+} ion

A neutral chromium atom has twenty-four electrons in the $1s^2\ 2s^2\ 2p^6\ 3s^2\ 3p^6\ 3d^5\ 4s^1$ configuration. When incorporated into a crystal lattice of a II-VI compound it will occupy a cation site, and two of its outer shell electrons will delocalize and contribute to the valence and conduction bands. The Cr^{2+} ion remains as a deep impurity in the semiconductor. To describe the state of the $3d$ shell, we shall follow the model description of a Cr^{2+} ion in a tetrahedral crystal field, proposed by Vallin *et al.*[1] The ground term is ^5D, with a total orbital momentum $L=2$ and total spin $S=2$, thus it has a 25-fold degeneracy. In a crystal field of cubic (tetrahedral T_d) symmetry it splits into a fifteen-fold degenerate orbital triplet $^5T_2$ and a tenfold degenerate orbital doublet ^5E, see Fig. 10. The splitting between the ground $^5T_2$ term and ^5E term is of the order of 5000 cm^{-1}. For the Cr^{2+} ion the ground term is the orbital triplet $^5T_2$, in contrast to the situation for the Fe^{2+} ion, where the order of the $^5T_2$ and ^5E levels is reversed.[22–25] The Fe^{2+} ion ground state, the spin-orbit split ^5E term, is rather insensitive to the Jahn-Teller effect[1] in contrast to the $^5T_2$ state $[E_{JT}(^5T_2) \gg E_{JT}(^5E)]$ and therefore the magnetic properties of Fe^{2+} ions, which result from this ^5E orbital doublet, can be described neglecting the Jahn-Teller effect.[10,26] For the Cr^{2+} ion however, the orbitally degenerate $^5T_2$ ground term undergoes a static, tetragonal Jahn-Teller distortion, which lowers the local symmetry and lifts the degeneracy of the ground level. This distortion is equivalent to a stress along one of the [100] crystal axes and leads to a further splitting of the ground term $^5T_2$ into a fivefold degenerate $^5B_2$ orbital singlet and the ^5E orbital doublet (located about 1000 cm^{-1} higher). The spin-orbit coupling results in subsequent level splittings. The $^5B_2$ term breaks up into a semidoublet (two nearby states Γ_1 and Γ_2), a doublet Γ_5 and a singlet Γ_4. The schematic diagram of the obtained energy levels for a Cr^{2+} ion in ZnSe, ZnS, or ZnTe is displayed in Fig. 10. It is equivalent to the schemes used in Refs. 1 and 24.

For ZnSe and ZnS the semidoublet is the ground state followed by the doublet and the singlet. For ZnTe the order is reversed; the singlet is the ground state, while the semidoublet is the highest in the series, see also Fig. 10. This inversion is caused by a strong covalency effect in ZnTe.[27] Because the spin-orbit interaction is rather weak compared to the Jahn-Teller distortion, the five lowest energy levels originating from the $^5B_2$ term, which are well separated from the higher energy levels, are split only by about 10 cm^{-1}. These five levels are mainly responsible for the magnetic and far-infrared properties, even at temperatures much higher than room temperature.

For a quantitative description of the electronic structure of the Cr^{2+} ion we use the following spin Hamiltonian:[11]

$$\mathcal{H}=\mathcal{H}_{cf}+\mathcal{H}_{JT}+\mathcal{H}_{so}, \tag{1}$$

with each successive term on the right-hand side representing a progressively weaker interaction. In Eq. (1) the tetrahedral (cubic) crystal field term is described by

$$\mathcal{H}_{cf}=B_4(\mathbf{O}_4^0+5\mathbf{O}_4^4), \tag{2}$$

according to Ref. 9, where the parameter B_4 is defined by the crystal-field splitting Δ following

$$\Delta=-120B_4. \tag{3}$$

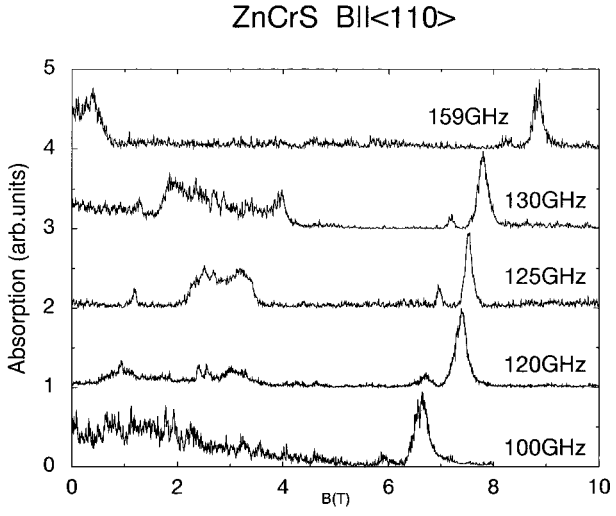

FIG. 9. Multifrequency EPR absorption spectra measured on $Zn_{1-x}Cr_xS$ for $B\|\langle 110\rangle$, $T=1.2$ K. All spectra are scaled and have offsets for clarity.

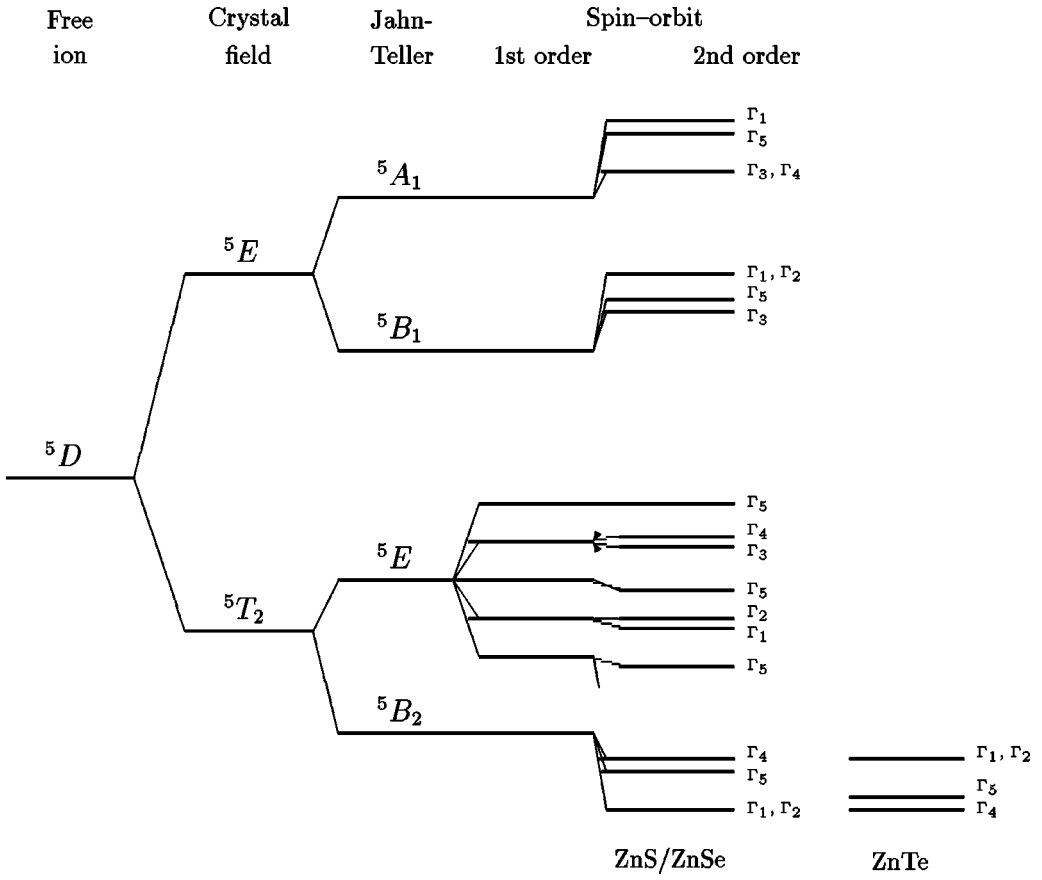

FIG. 10. Splitting of the ^5D state of a Cr^{2+} ion in the absence of a magnetic field. The energy level scheme is calculated with a crystal field in D_{2d} symmetry, a tetragonal Jahn-Teller distortion and second order spin-orbit interaction (following Ref. 1).

For further analysis, after selecting the spin orbit and Jahn-Teller parameters, Δ was slightly adjusted to obtain an energy difference between the lowest level of the $^5B_1$ quintet and the ground state exactly matching the observed near infrared transition,[1] denoted as the zero phonon line. $\mathcal{H}_{JT}$ represents the tetragonal static Jahn-Teller distortion

$$\mathcal{H}_{JT} = B_4^0(5\mathbf{O}_2^0 + \mathbf{O}_4^0), \tag{4}$$

where the parameter B_4^0 is related to the Jahn-Teller energy $E_{JT}(^5T_2)$ of the $^5T_2$ term by

$$E_{JT}(^5T_2) = -35B_4^0 \tag{5}$$

assuming that the Jahn-Teller splitting between the $^5B_2$ and ^5E levels is $3E_{JT}(^5T_2)$. We neglected the $E_{JT}(^5E)$ term, since the energy splitting of the ^5E term, as reported by Vallin *et al.*,[1] is rather small and does not influence the energy levels of the $^5B_2$ quintet. The spin-orbit coupling term is given by

$$\mathcal{H}_{so} = \lambda \mathbf{L}\cdot\mathbf{S}, \tag{6}$$

where, instead of using one free ion spin-orbit coupling parameter,[24] we used three different parameters. This reflects the fact that the strength of the spin-orbit coupling may depend on admixture between the Cr $3d$ wave functions and the ligand wave functions, which is different for the ^5E and $^5T_2$ states.[28] Therefore, three different parameters λ_{TT}, λ_{TE}, and λ_{EE} are defined:

$$\begin{aligned}
\langle \psi_T|\mathcal{H}_{so}|\psi_T\rangle &= \lambda_{TT}\langle \psi_T|\mathbf{L}\cdot\mathbf{S}|\psi_T\rangle,\\
\langle \psi_T|\mathcal{H}_{so}|\psi_E\rangle &= \lambda_{TE}\langle \psi_T|\mathbf{L}\cdot\mathbf{S}|\psi_E\rangle,\\
\langle \psi_E|\mathcal{H}_{so}|\psi_E\rangle &= \lambda_{EE}\langle \psi_E|\mathbf{L}\cdot\mathbf{S}|\psi_E\rangle
\end{aligned} \tag{7}$$

where ψ_E and ψ_T are the wave functions of ^5E and $^5T_2$ subspaces respectively.[29] In contrast to Vallin *et al.*,[1] we do not construct a simplyfied effective Hamiltonian, but solve the full Hamiltonian numerically. The set of values for λ, which we used for matching to the low-energy levels of the $^5B_2$ term is not unique. For ZnS and ZnSe it is also possible to obtain a good description of the energy levels with one spin-orbit coupling parameter, if the Jahn-Teller energy is adopted from Vallin *et al.*[1] For a Jahn-Teller energy of about $E_{JT}(^5T_2) = 300\ \mathrm{cm}^{-1}$ (Refs. 31 and 32) three different λ's must be used to obtain a good match between experimental data and our description. However λ_{EE} has a weak influence on the $^5B_2$ levels, and therefore we can use a free ion value. The spin-spin interaction is neglected, because it is two orders of magnitude smaller than the spin-orbit interaction. The wave functions $|\psi\rangle$ are chosen as products of an orbital wave function $|m_l\rangle$, and a spin wave function $|m_s\rangle$: $|\psi\rangle = |m_l\rangle|m_s\rangle$.[1,11,30] For diagonalizing $\mathcal{H}_{cf}$ and $\mathcal{H}_{JT}$ we used a set of five orbital wave functions $|m_l\rangle$ as summarized in Table I. These orbital wave functions have energy eigenvalues as listed in the same table, expressed in terms of the crystal field and Jahn-Teller parameters B_4 and B_4^0, and can be compared with Fig. 10. Together with the spin wave func-

TABLE I. Energy levels from Fig. 10 with their corresponding orbital wave functions $|m_l\rangle$. These wave functions are used to diagonalize $\mathcal{H}_{cf}$ and $\mathcal{H}_{JT}$. The resulting energy eigenvalues are expressed in terms of the parameters B_4 and B_4^0 (Ref. 9).

Crystal field	Jahn-Teller	$\|m_l\rangle$	E
^5E	$^5A_1$	$\|0\rangle$	$72\,B_4 + 42\,B_4^0$
$\|\psi_E\rangle$	$^5B_1$	$(\|2\rangle+\|-2\rangle)/\sqrt{2}$	$72\,B_4 + 42\,B_4^0$
$^5T_2$	^5E	$\|1\rangle$	$-48\,B_4 - 63\,B_4^0$
$\|\psi_T\rangle$	^5E	$\|-1\rangle$	$-48\,B_4 - 63\,B_4^0$
	$^5B_2$	$(\|2\rangle-\|-2\rangle)/\sqrt{2}$	$-48\,B_4 + 42\,B_4^0$

tions $|m_s\rangle$ they form the basis, which was used to calculate the matrix elements of the spin-orbit coupling term $\mathcal{H}_{so}$ and the Zeeman term $\mathcal{H}_B$ described in the next section.

B. EPR transitions in a magnetic field

A magnetic field lifts the degeneracy of the remaining doublets and adds some interaction between the levels. The effect of an external magnetic field is described by the Zeeman term

$$\mathcal{H}_B = \mu_B(\mathbf{L}+2\mathbf{S})\mathbf{B}, \tag{8}$$

where μ_B is the Bohr magneton and **B** the magnetic-field vector. The energy levels as a function of the magnetic field are then calculated by numerical diagonalization of the total 25×25 spin Hamiltonian matrix. This matrix is parameterized by, B_4, B_4^0, λ_{TT}, λ_{TE}, and λ_{EE}, as described in the previous section.[29] The parameters were evaluated fitting the calculated energies to the experimental data.

At millimeter wave energies there are several allowed optical transitions between the various spin-orbit-split levels within the $^5B_2$ state. For polarization of the millimeter wave magnetic field perpendicular to the static magnetic field, which was used in our experiment, electron paramagnetic resonance is observed for magnetic dipole transitions, $\Delta m_s = \pm 1$.[1,27] Neglecting any ligand admixture affecting the Cr^{2+} orbital momentum (m_l) and spin (m_s) quantum numbers, and assuming a constant equally distributed Cr^{2+} center population,[11] one can also calculate relative transition intensities according to

$$I_{rel} = |\langle \psi_f|\mathcal{S}_x,\mathcal{S}_y|\psi_i\rangle|^2 \tag{9}$$

where ψ_f and ψ_i are the wave functions of the final and initial Cr^{2+} states, respectively.

When a magnetic field is applied along the $\langle 100\rangle$ direction, parallel to a Jahn-Teller distortion axis, the five lowest-lying energy levels, the semidoublet (Γ_1, Γ_2) ($m_s=\pm2$), the doublet Γ_5 ($m_s=\pm1$) and the singlet Γ_4 ($m_s=0$), start interacting with their corresponding m_s energy levels from the $^5B_1$ state, but not with each other,[27] in which case the spin quantum number m_s is conserved. For the ''0°'' configuration center this means that there are allowed transitions between the (Γ_1, Γ_2) and Γ_5 and between the Γ_5 and Γ_4 levels, see also Fig. 11. The interaction affects the effective g value, which depends on the spin-orbit mixing of the $^5B_1$ wave functions into the $^5B_2$ ground state.[28] The linear dependence can be seen in the calculated energy levels in Fig. 11 for the ''0°'' configuration. When there is a nonzero angle between the magnetic-field direction and the Jahn-Teller distortion axis, the (Γ_1, Γ_2), Γ_5 and Γ_4 levels start interacting with each other and with other higher-lying energy levels. In this case the spin quantum number m_s of the energy levels is not conserved anymore, and as a result, the magnetic field dependence shows a very non-linear behavior, see Figs. 12 and 13. For these configurations (''45°,'' ''54.7°'' and ''90°'') the wave functions of the corresponding energy levels are composed of different $|m_s\rangle$ contributions as function of the magnetic field, in which case different transitions are allowed. An estimation of the expected relative intensities of the resonances can be calculated by Eq. (9).

V. DISCUSSION

In this section, we will analyze the magnetic-field positions of the resonances we observed, and compare them with the described theoretical predictions. The positions of the absorption lines are determined and plotted in an energy versus magnetic-field diagram for different magnetic-field orientations. In all these diagrams the lines (solid and dashed) represent the energy levels, relative to the ground level energy, which are the results of the crystal-field calculations for the Cr^{2+} center in different configurations. The dotted lines give the energy differences between higher-lying energy levels. Finally, we will summarize the parameters used to match our model description of the low-energy levels with the ob-

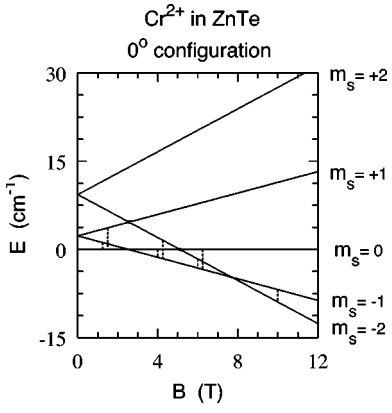

FIG. 11. Calculated energy levels of $Zn_{1-x}Cr_xTe$ as function of the magnetic field B, which is parallel to the Jahn-Teller distortion axis (''0°'' configuration). The thick solid line represents the changing ground state of the Cr^{2+} ion, while the other lines are excited states. All energy levels are labeled by their corresponding quantum number m_s. The dashed lines indicate the allowed magnetic dipole transitions, $\Delta m_s = \pm 1$.

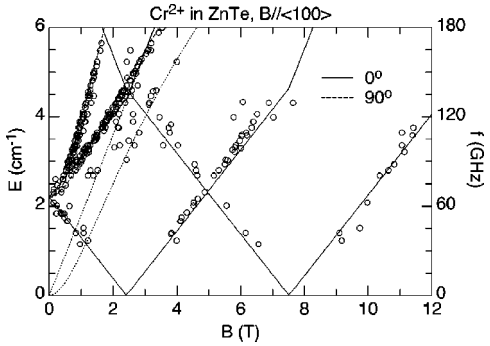

FIG. 12. Transition energies of $Zn_{1-x}Cr_xTe$ derived from EPR positions for several different energies (frequencies) as function of the magnetic field B parallel to the $\langle 100\rangle$ direction. The dashed and solid lines are the calculated energies of transitions from the ground state, see also Fig. 11, while the dotted lines represent transitions between excited states. The solid lines correspond to transition energies for the magnetic field parallel to the Jahn-Teller distortion axis, the ''0°'' configuration, and the dashed lines to the ''90°'' configuration.

served experimental data, and compare these to other used descriptions.[1,24]

A. $Zn_{1-x}Cr_xTe$

In Fig. 12, the positions of the observed absorption lines at $T \approx 1.2$ K are plotted in an energy versus magnetic-field diagram. The parameters used in the model calculation are: $B_4 = -41.18\ cm^{-1}$, $B_4^0 = -9.14\ cm^{-1}$, $\lambda_{TT} = -51.0\ cm^{-1}$, $\lambda_{TE} = +30.0\ cm^{-1}$, and $\lambda_{EE} = +57.0\ cm^{-1}$.

The ground state at zero-magnetic field is the $m_s = 0$ level (Γ_4, see also Figs. 10 and 11). The $m_s = \pm 1$ levels (Γ_5) are $2.3\ cm^{-1}$ higher in energy. Note that in the case of $Zn_{1-x}Cr_xTe$ the order of the five low-lying energy levels is reversed as compared to $Zn_{1-x}Cr_xSe$ and $Zn_{1-x}Cr_xS$.

As function of the magnetic field, the ground state for the configuration in which the magnetic field is parallel to the Jahn-Teller distortion axis, see Fig. 11, changes at $B = 2.5$ T from the singlet state $m_s = 0$ to a $m_s = -1$ level, and at $B = 7.8$ T from the $m_s = -1$ to the $m_s = -2$ state. These changes of the ground state result in a steplike change of the ground level spin, and give rise to steps in the magnetic-field dependence of the magnetization.[11] At low-magnetic fields and for the ''0°'' configuration we clearly see the $\Delta m_s = \pm 1$ transitions, while $\Delta m_s = \pm 2$ transitions are not observed. At intermediate magnetic fields, $2.5\ T < B < 7.8\ T$, the transitions between the ground level ($m_s = -1$) and the first and second excited states ($m_s = 0$ and $m_s = -2$) are observable, although weaker. At high-magnetic fields no transitions are observed between the ground state ($m_s = -2$) and the second excited state ($m_s = 0$), which is in agreement with theory (the energy level around 8 T between 4.5 cm^{-1} and 6 cm^{-1}). The transition to the first excited state is observed but only very weak, in contrast to the calculated relative intensity, which should be the same as for the low field first excited state transition. This can give an indication for a redistribution of the Cr^{2+} center population in magnetic fields, as was also suggested from magnetization measurements,[11] and results in less ''0°'' centers at high-magnetic fields. Transitions from the ground state to the excited states from the Γ_5 doublet ($m_s = \pm 1$) for the two ''90°'' configuration centers are clearly observed.

A few observed absorption lines may correspond to transitions between excited states, which are calculated and shown in Fig. 12 as the dotted lines corresponding to transitions between the split levels of the Γ_5 doublet for the two different configurations. The increasing number of these lines with increasing temperature,[29] confirms that these transitions originate from excited states. Figure 13 shows the observed resonance line positions in a magnetic field along the $\langle 110\rangle$ direction. The transitions from the ground state singlet to the Γ_5 doublet are clearly seen for the two different configurations. As discussed before the double resonances originate from a slight misorientation of the crystal, which can also be seen in Fig. 13 by double points on one level for the same frequency. We note that, in contrast to our experimental technique, a single frequency EPR measurement cannot be decisive for the exact energy level structure due to the nonlinear magnetic-field dependency of the energy levels and the large zero-field splitting of $2.3\ cm^{-1}$ (69 GHz).

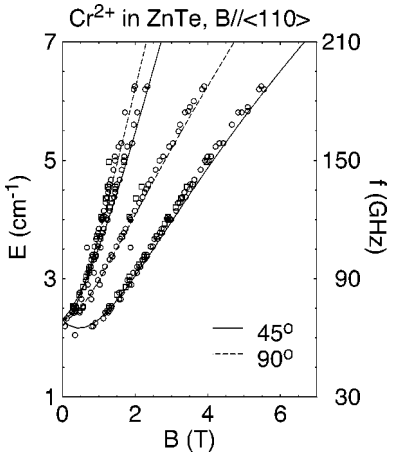

FIG. 13. Cr^{2+} transition energy versus magnetic field for $B \| \langle 110\rangle$ axis giving rise to two orientationally different Cr centers (''45°'' and ''90°'' configuration). Data taken on two different samples are represented by ○ and □, whereas the lines are results of the crystal-field calculation of the energy levels.

B. $Zn_{1-x}Cr_xSe$

The resonance positions from Fig. 7 were determined and are shown in Fig. 14 together with the energy levels from the model calculations. The used calculation parameters are: $B_4 = -41.33\ cm^{-1}$, $B_4^0 = -9.71\ cm^{-1}$, $\lambda_{TT} = +33.5\ cm^{-1}$, $\lambda_{TE} = +65.0\ cm^{-1}$, and $\lambda_{EE} = +57.0\ cm^{-1}$. Note that now the ($\Gamma_1$, Γ_2) semidoublet ($m_s = \pm 2$) is the ground state, and the first excited state is the Γ_4 doublet ($m_s = \pm 1$).

In Fig. 14 one can notice that for the ''0°'' configuration we do not observe any resonance corresponding with the transition between the ground state and the first excited state, which is in agreement with $\Delta m_s = \pm 4$ forbidden transitions and no interaction between the five low-lying states induced by the magnetic field. For the ''90°'' configuration centers on the contrary we can observe these transitions with increasing field since there is considerable interaction between the different m_s states, not conserving the m_s quantum num-

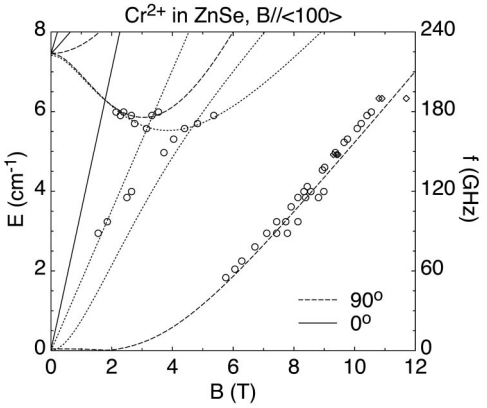

FIG. 14. Energy versus magnetic field diagram displaying the transition energy from the EPR measurements on $Zn_{1-x}Cr_xSe$ as function of the magnetic field $\mathbf{B}\|\langle 100\rangle$. For the two different configurations the calculated energy levels are shown as solid, respectively dashed lines. The dotted lines represent transitions between excited states.

ber. At higher energies several additional resonances are observed, see Figs. 7 and 14. These resonances, observed at 167 GHz for example, are transitions between the first excited state [one of the (Γ_1, Γ_2) levels] and the lowest state from the Γ_4 doublet. The opposite dispersion curves reflect the slope of the energy versus magnetic-field dependence as can be seen in Fig. 14. When the frequency is slightly increased to 179 GHz the former two resonances move further apart, and the resonance at higher field loses intensity due to a lower population of the initial excited state in higher fields (larger splitting between the ground state and the first excited level). In between those two resonances two new ones appear, being transitions from the ground state. The other points correspond to weaker resonances and are transitions between the higher lying excited states of the Γ_4 doublet, as can be seen in Fig. 14.

For the magnetic field along the $\langle 111\rangle$ direction, see Fig. 15, where all the Cr^{2+} centers are in the ''54.7°'' configuration, the interaction between the levels of the $^5B_2$ state is weaker than in the ''90°'' configuration and therefore transitions from the ground state to the first excited state are hardly observed. The resonances that are observed, are between excited states.

C. $Zn_{1-x}Cr_xS$

The absorption lines from the EPR experiments on $Zn_{1-x}Cr_xS$ with the magnetic field along the $\langle 110\rangle$ direction are displayed in Fig. 16. The energy level configuration is approximately the same as for $Zn_{1-x}Cr_xSe$, except the parameters for the calculation are now: $B_4 = -43.47\ cm^{-1}$, $B_4^0 = -8.75\ cm^{-1}$, $\lambda_{TT} = +9.1\ cm^{-1}$, $\lambda_{TE} = +50.0\ cm^{-1}$, and $\lambda_{EE} = +57.0\ cm^{-1}$. Again the resonances from transitions between ground and excited state are much clearer in the ''90°'' configuration than in the ''45°'' configuration due to a stronger interaction between the low-energy levels if the Jahn-Teller distortion axis is perpendicular to the applied magnetic field. The doubling of the high-field resonances can be ascribed to different hexagonal stresses as explained earlier.

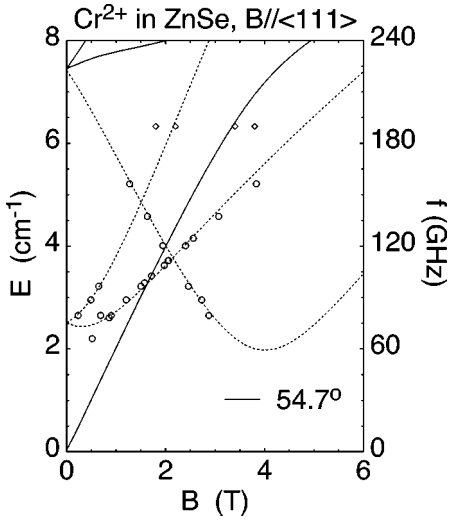

FIG. 15. Magnetic-field dependence of the calculated energy levels of $Zn_{1-x}Cr_xSe$ (solid lines) for the field along the $\langle 111\rangle$ direction. The dotted lines correspond to transitions between higher lying energy levels. The open circles represent the EPR data points from several different frequency measurements.

D. Comparison

The parameter values of the full Hamiltonian we obtained from numerically fitting the energy levels of the $^5B_2$ quintet to the experimentally observed resonances for the different host materials we studied, are summarized in Table II.

We observe that a good description of the five lowest energy levels can be obtained with a different set of spin-orbit and Jahn-Teller parameters compared with earlier results. For the Jahn-Teller energies three different λ parameters are necessary, in agreement with Vallin *et al.*[27] In Vallins case the Jahn-Teller energy is larger, the Cr^{2+} displacement in the host lattice will be larger, and to obtain the same energy level scheme the spin-orbit interaction parameters must increase as well to account for the smaller overlap between the Cr^{2+} $3d$ wave functions and the ligand wave

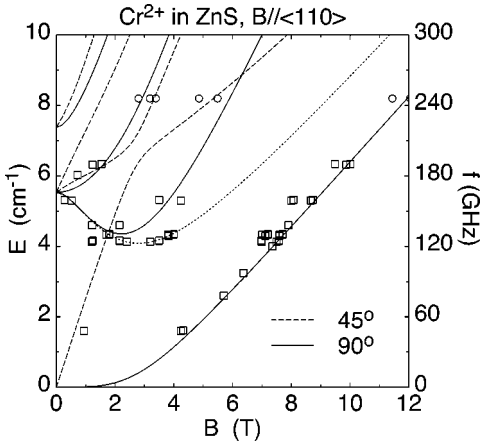

FIG. 16. The experimentally observed absorption line positions for $Zn_{1-x}Cr_xS$ in the energy versus magnetic-field diagram for the magnetic field parallel to the $\langle 110\rangle$ axis. Dashed and solid lines are the calculated energy levels, dotted lines are transition energies between excited states and the squares are the EPR data points. (Open circles are FIR laser measurements from Ref. 33.)

TABLE II. Parameters B_4, B_4^0, λ_{TT}, λ_{TE}, and λ_{EE}, used in our energy level calculations, together with the corresponding crystal field energy Δ, the Jahn-Teller energy E_{JT}, and the zero field splitting parameter D. All energies are in cm^{-1}.

Crystal	B_4	Δ	B_4^0	E_{JT}	λ_{TT}	λ_{TE}	λ_{EE}	D
ZnCrS	−43.47	5216	−8.75	306.3	+9.1	+50.0	+57.0	−1.84
ZnCrSe	−41.33	4960	−9.71	340.0	+33.5	+65.0	+57.0	−2.48
ZnCrTe	−41.18	4942	−9.14	320.0	−51.0	+30.0	+57.0	+2.29

functions. Compared to Vallin *et al.*,[1,27] who used an effective Hamiltonian description, we used larger crystal-field parameters and smaller Jahn-Teller distortion energies, which are closer to the experimental values found in Refs. 32 and 31. Similar to Vallin *et al.*[27] we used three spin-orbit parameters to account for the different admixture of $^5T_2$ and ^5E states with the ligand fields.[28] Since the Jahn-Teller energies of Vallin *et al.* are larger, their spin-orbit parameters are also larger for ZnS and ZnTe in order to obtain an equal zero-field splitting value D. For ZnSe Vallin *et al.* need an unrealistic negative spin orbit coupling parameter λ_{TT}, which is not consistent with the Jahn-Teller energies and the energy level scheme for Cr^{2+} in ZnS with respect to ZnSe.

Comparing our data with earlier results of Colignon *et al.*,[24] we used slightly higher crystal field parameters, but neglected the spin-spin interaction term in the Hamiltonian and diversified the spin-orbit parameter, where Colignon used a too general approach, using the free ion spin-orbit parameter value. They also find a large difference in the Jahn-Teller energy values over the three compounds, while we used approximately the same values for all three host lattices.

VI. CONCLUSION

To conclude, our high magnetic field EPR technique is a very effective tool to study the complex behavior of Cr^{2+} energy levels in ZnTe, ZnSe, and ZnS host lattices. With the unique combination of tunable frequency and simultaneous absorption and dispersion measurements, we can follow the magnetic-field dependence of the lowest lying energy levels over a broad range of frequencies and magnetic fields, and thus measure more points at lower energies. These electronic states, which are directly responsible for the macroscopic magnetization can be well described by a crystal-field model incorporating a Jahn-Teller distortion and a complete spin-orbit coupling description. We provided a detailed analysis of the symmetry and magnetic-field dependence of low-lying Cr^{2+} levels and we discussed various theoretical models used for their description. We determined the spin Hamiltonian parameters for all compounds we studied. The parameter set, which we found by numerically solving the full spin Hamiltonian differs from Vallin *et al.*, who use an effective Hamiltonian (fenomenological description) in the smaller values of Jahn-Teller energy and spin-orbit coupling parameters. Compared to Colignon *et al.* we used a more realistic model with three different values for spin-orbit parameters, and obtained a more uniform value for the Jahn-Teller energy for the three host lattices. The observed increase of the spin-orbit parameter with anion atomic mass corresponds to the increasing overlap with the ligand wave functions and the increasing ion radius of the ligand ions.

ACKNOWLEDGMENTS

This work is part of the research program of the Stichting voor Fundamenteel Onderzoek der Materie (FOM), which is financially supported by the Nederlandse Organisatie voor Wetenschappelijk Onderzoek (NWO). This work is also supported by The State Committee of Scientific Research (Poland) and by the European Commission under Contract Nos. CIPD-CT94-0767 and CIPA-CT93-0032.

*Present address: ASML, Development & Engineering, De Run 1110, NL-5503 LA, Veldhoven, the Netherlands.

[1] J. T. Vallin, G. A. Slack, S. Roberts, and A. E. Hughes, Phys. Rev. B **2**, 4313 (1970).

[2] *Diluted Magnetic Semiconductors*, edited by J.K. Furdyna and J. Kossut, Semiconductors and Semimetals Vol. 25, (Academic Press, London, 1988).

[3] *Diluted Magnetic Semiconductors*, edited by M. Balkanski and M. Averous (Plenum Press, New York, 1991).

[4] J. Kossut and W. Dobrowolski, in *Handbook of Magnetic Materials*, edited by K.H.J. Buschow (North-Holland, Amsterdam, 1993), Vol. 7, p. 231.

[5] J.A. Gaj, J. Ginter, and R.R. Gałązka, Phys. Status Solidi B **89**, 655 (1978).

[6] W. Mac, Nguyen The Khoi, A. Twardowski, J.A. Gaj, and M. Demianiuk, Phys. Rev. Lett. **71**, 2327 (1993).

[7] J. Mycielski, Solid State Commun. **60**, 165 (1986).

[8] S. Oseroff and P.H. Keesom, in *Diluted Magnetic Semiconductors* (Ref. 2).

[9] A. Abragam and B. Bleaney, *Electron Paramagnetic Resonance of Transition Metal Ions* (Clarendon Press, Oxford, 1970).

[10] A. Twardowski, J. Appl. Phys. **67**, 5108 (1990).

[11] W. Mac, A. Twardowski, P.T.J. Eggenkamp, H.J.M. Swagten, Y. Shapira, and M. Demianiuk, Phys. Rev. B **50**, 14 144 (1994).

[12] A. Twardowski, T. Fries, Y. Shapira, P.T.J. Eggenkamp, H.J.M. Swagten, and M. Demianiuk, J. Appl. Phys. **73**, 5745 (1993).

[13] P. Goy, M. Gross, and J.M. Raimond, in *Proceedings of the 15h International Conference on IR and mm Waves, Orlando, Florida, 1990*, edited by R.J. Temkin (Plenum Press, New York, 1990), p. 172.

[14] R.S. Alger, *Electron Spin Resonance: Techniques and Applications* (Interscience Publishers, New York, 1968).

[15] C.P. Poole, *Electron Spin Resonance* (Interscience Publishers, New York, 1967).

[16] M.E.J. Boonman, J.A.A.J. Perenboom, P.J.M van Bentum, A. Wittlin, J.C. Maan, W. Mac, A. Twardowski, S.O. Hill, R. Kato,

H. Sawa, and S. Aonuma, in *High Magnetic Fields in the Physics of Semiconductors*, edited by G. Landwehr and W. Ossau (World Scientific, Singapore, 1997), p. 777.
[17] M.E.J. Boonman, Ph.D. thesis, Nijmegen University, 1998.
[18] W. Giriat and J.K. Furdyna, in *Diluted Magnetic Semiconductors* (Ref. 2).
[19] We use in this work notations in which the crystallographic directions are named as for corresponding directions in the zinc blende structure, i.e., the threefold axis is called ⟨111⟩.
[20] M.E.J. Boonman, W. Mac, A. Twardowski, A. Wittlin, and M. Demianiuk, Acta Phys. Pol. A **88**, 829 (1995).
[21] W. Mac, A. Twardowski, M.E.J. Boonman, A. Wittlin, R. Krevet, M. von Ortenberg, and M. Demianiuk, Physica B **211**, 384 (1995).
[22] G.A. Slack, S. Roberts, and J.T. Vallin, Phys. Rev. **187**, 551 (1969).
[23] W. Low and M. Weger, Phys. Rev. **118**, 1119 (1960).
[24] D. Colignon, E. Kartheuser, S. Rodriguez, and M. Villeret, J. Cryst. Growth **159**, 875 (1996).
[25] E. Kartheuser, S. Rodriguez, and M. Villeret, Phys. Rev. B **48**, 14 127 (1993).
[26] H.J.M. Swagten, A. Twardowski, W.J.M. de Jonge, and M. Demianiuk, Phys. Rev. B **39**, 2568 (1989).
[27] J.T. Vallin and G.D. Watkins, Phys. Rev. B **9**, 2051 (1974).
[28] De-Hua Li, Fu-Zhen Li, and Yi-Yang Zhou, Solid State Commun. **105**, 59 (1997).
[29] W. Mac, Ph.D. thesis, Warsaw University, 1996.
[30] G.A. Slack, S. Roberts, and J.T. Vallin, Phys. Rev. **187**, 511 (1969).
[31] M. Kamińska and J.M. Baranowski, J. Phys. C **12**, 2197 (1979).
[32] B. Nygren, J.T. Vallin, and G.A. Slack, Solid State Commun. **11**, 35 (1972).
[33] R. Krevet, A. Twardowski, M. von Ortenberg, W. Mac, and M. Demianiuk, Solid State Commun. **87**, 709 (1993).